Title

Inferred rheological structure and mantle conditions from postseismic deformation following the 2010 Mw 7.2 El Mayor-Cucapah Earthquake

Journal

Geophysical Journal International, 213(3)

ISSN

0956-540X

Authors

Dickinson-Lovell, Haylee
Huang, Mong-Han
Freed, Andrew M
et al.

Publication Date

2018-06-01

DOI

10.1093/gji/ggx546

Peer reviewed

Inferred rheological structure and mantle conditions from postseismic deformation following the 2010 M_w 7.2 El Mayor-Cucapah Earthquake

Haylee Dickinson-Lovell, Mong-Han Huang, Andrew M Freed, Eric Fielding, Roland Bürgmann, Christopher Andronicos

SUMMARY

The 2010 M_w7.2 El Mayor-Cucapah earthquake provides a unique target of postseismic study as deformation extends across several distinct geological provinces, including the cold Mesozoic arc crust of the Peninsular Ranges and newly formed, hot, extending lithosphere within the Salton Trough. We use five years of global positioning system measurements to invert for afterslip and constrain a 3-D finite-element model that simulates viscoelastic relaxation. We find that afterslip cannot readily explain far-field displacements (more than 50 km from the epicentre). These displacements are best explained by viscoelastic relaxation of a horizontally and vertically heterogeneous lower crust and upper mantle. Lower viscosities beneath the Salton Trough compared to the Peninsular Ranges and other surrounding regions are consistent with inferred differences in the respective geotherms. Our inferred viscosity structure suggests that the depth of the Lithosphere/Asthenosphere Boundary (LAB) is ~65 km below the Peninsular Ranges and ~32 km beneath the Salton Trough. These depths are shallower than the corresponding seismic LAB. This suggests that the onset of partial melting in peridotite may control the depth to the base of the mechanical lithosphere. In contrast, the seismic LAB may correspond to an increase in the partial melt percentage associated with the change from a conductive to an adiabatic geotherm.

Keywords: Creep and deformation, Transient deformation, Rheology: crust and lithosphere

1 INTRODUCTION

Southern California and Northwestern Mexico contain a geological transition of the Pacific-North American plate boundary from right-lateral motion on the San Andreas Fault system to oceanic spreading linking transform fault segments in the Gulf of California. Nearly all of the plate-boundary shear strain associated with the ~50 mm yr^{-1} relative motion between the Pacific and North American plates is accommodated in the Salton Trough. This region of transtension produces a high rate of seismicity, averaging approximately one large earthquake (>M_w 6.2) every 12 yr (Fletcher *et al.*2014). The 2010 April 4 M_w 7.2 El Mayor-Cucapah (EMC) earthquake ruptured ~120 km on at least eight major en echelon fault strands. The strands overlap and are generally left-stepping (at least at the surface) within the Salton Trough (Fletcher *et al.*2014), some of which were previously unmapped. Coseismic slip, which was modeled based on a

geometric simplification of these fault segments (Huang *et al.*2017), modified the stress field throughout the region.

In the years following the EMC earthquake, postseismic surface deformation was recorded on an array of continuous global positioning system (CGPS) stations north of the US/Mexico border (Fig. 1), a combination of EarthScope Plate Boundary Observatory and USGS sites. Postseismic deformation generally arises from a combination of viscoelastic relaxation of a viscously weak lower crust and/or upper mantle, aseismic slip within and beyond the fault rupture surface (afterslip), and fluid flow induced by coseismic pressure changes (poroelastic rebound). Thus, these displacements can be used to constrain the rheological properties of a region. Postseismic displacements following the EMC earthquake are the first to span an active transtensional transform system characterized by high heat flow, thinned crust, magmatic intrusions and young sedimentary basins, providing a unique opportunity to explore the associated viscoelastic structure and its implications for such a deformation environment.

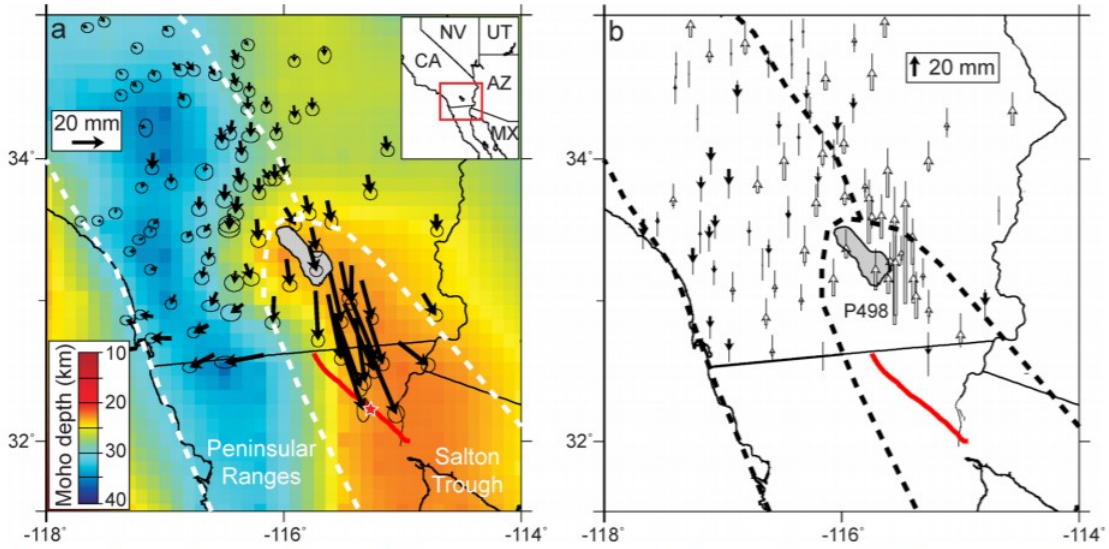

Figure 1. 5-yr cumulative (a) horizontal and (b) vertical GPS observed postseismic surface displacements following the El Mayor-Cucapah earthquake. The surface rupture is shown as a red line with the epicentre as a star. Colour contour in (b) shows the depth of the Moho. Dashed lines outline the Salton Trough and Peninsular Ranges provinces.

Previous studies of the broad pattern of postseismic displacements (extending more than 50 km from the rupture surface) in the first few (1.5–3) yr following the EMC earthquake have concluded that it results from the relaxation of a horizontally and vertically varying viscoelastic structure across the region (Pollitz *et al.*2012; Rollins *et al.*2015). A study using 5 yr of postseismic data confirmed that broad postseismic displacements were due primarily to viscoelastic relaxation in the upper mantle (Hines & Hetland 2016). This study did not, however, explore how horizontal rheological heterogeneities may have influenced postseismic relaxation. Here, we develop a fully 3-D model of postseismic relaxation following the EMC earthquake that relies on 5 yr of postseismic data to explore the

influence of lateral heterogeneity across this transtensional transform system and estimate the first-order vertical viscosity structure within and outside of the Salton Trough region. We use this model to examine the potential contributions of afterslip to postseismic displacements, evaluate the heterogeneous nature of the viscoelastic structure implied by these displacements, and explore what this viscoelastic structure implies about the mineralogy and deformation conditions of the region. In particular, we are interested in determining whether inferred horizontal changes in the viscosity structure are a result of significant variations in temperature, as indicated by heat flow (e.g. Blackwell *et al.*2011), or due to mineralogical, water content or melt differences across a region that spans both active spreading and continental provinces. Such compositional differences may be expected across the region since the crust beneath the Salton Trough has been affected by large magnitude extension and magmatic additions following formation of the Peninsular Ranges batholith (Lachenbruch *et al.*1985; Schmitt & Vazquez 2006).

2 GEODETIC CONSTRAINTS

We obtained daily position time-series of 116 CGPS stations from the Nevada Geodetic Laboratory (http://geodesy.unr.edu). In order to calculate the postseismic displacements, we first use ~5 yr of pre-EMC GPS time-series (2005–2010) to estimate secular, annual and semi-annual deformation (primarily interseismic motion) terms by fitting the equation,

$$\begin{aligned} U_{E,N,Z}(t) = {} & A_{E,N,Z} + B_{E,N,Z}t + C_{E,N,Z}\sin(2\pi t) \\ & + D_{E,N,Z}\cos(2\pi t) + E_{E,N,Z}\sin(4\pi t) \\ & + F_{E,N,Z}\cos(4\pi t) \end{aligned} \quad (1)$$

where $U_{E,N,Z}(t)$ is the time-dependent displacement of east, north and vertical components, respectively, before the EMC earthquake, A is the reference position, B is the secular velocity, C and D are the coefficients of annual displacement and E and F are the coefficients of semi-annual displacement. We estimate the coefficients using least squares for each station, and then subtract these contributions from the post-EMC time-series. This procedure allows us to estimate the postseismic displacement from the day immediately following the EMC earthquake through ~5 yr of cumulative postseismic displacement (Fig. 2). Many of the postseismic displacement time-series were influenced by the 2010 June 15 M_w 5.7 Ocotillo aftershock and the 2012 M5 Brawley seismic swarm that both occurred south of the Salton Sea (Wei *et al.*2013, 2015). These influences were removed using offset estimates from UNAVCO (https://www.unavco.org/highlights/2010/M7.2-Baja.html for Oco-tillo and https://www.unavco.org/highlights/2012/brawley.html for Brawley).

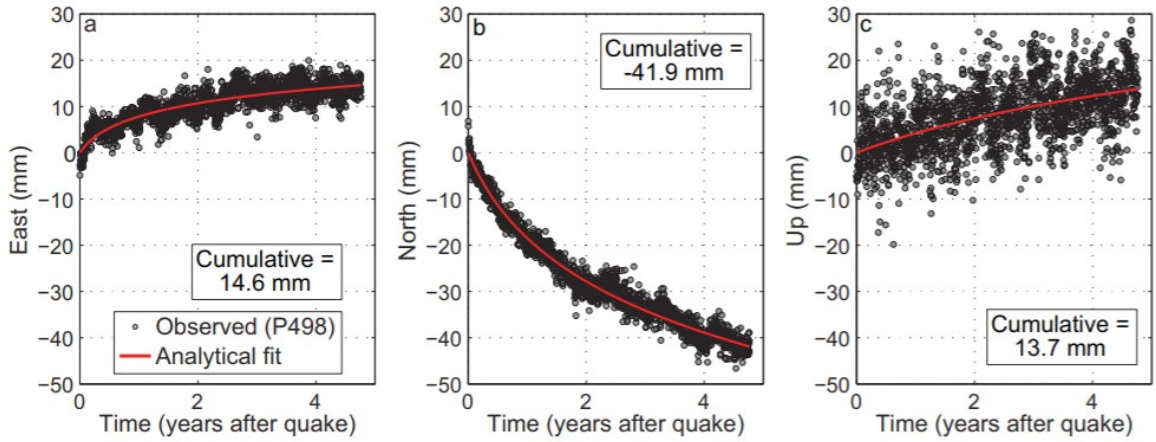

Figure 2. Observed postseismic displacement time-series and analytical fitting using eq. (2) for station P498. The relaxation time τ for P498 is one year. See Fig. 1 for station location.

To estimate the cumulative postseismic displacement of the three components for each CGPS station, we fit each 5-yr time-series with logarithmic functions,

$$U_{E,N,Z}(t) = V_{E,N,Z} \log\left(1 + \frac{t - t_o}{\tau}\right), \qquad (2)$$

where $V_{E,N,Z}$ is the amplitude of the logarithmic function in east, north and vertical components, t_o is the earthquake time and τ is the relaxation time. For the EMC earthquake, the relaxation time in the logarithmic function for postseismic displacement is found to be between a few days to years depending on the location of GPS stations. Fig. 2 shows an example for fitting the three components of CGPS station P498 with a relaxation time of 1 yr.

The cumulative postseismic deformation pattern (Fig. 1a) is similar to that of the coseismic displacement field (Fig. 3), displaying right-lateral deformation. Such a relationship is often observed (e.g. Freed *et al.*2006a, 2007), as postseismic deformation relieves stresses induced by the earthquake. Vertical postseismic displacements (Fig. 1b) generally reveal uplift throughout the region, with the greatest uplift occurring in the Salton Trough region. As is often the case, the signal-to-noise ratio is much lower for the GPS observed postseismic vertical displacements due to its larger error and contributions from non-tectonic processes such as changes in local water levels.

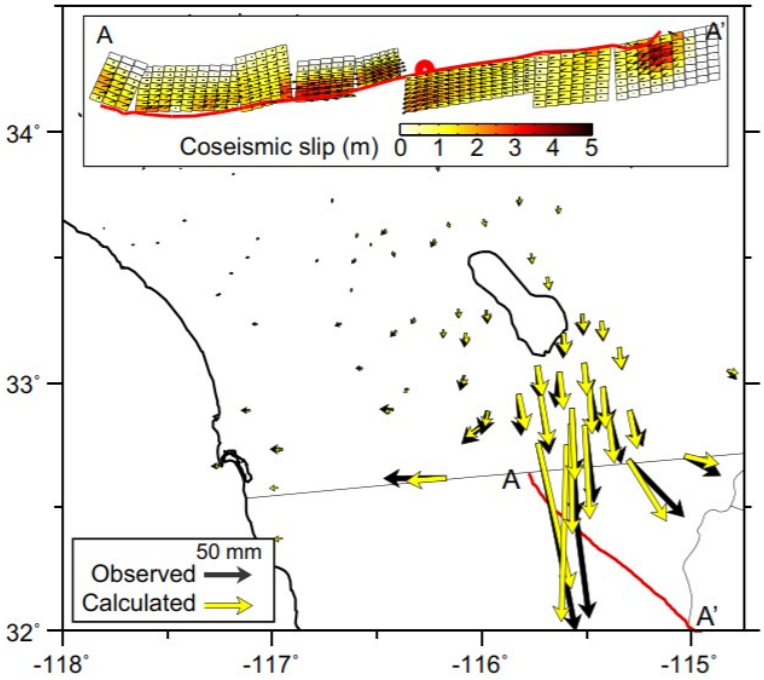

Figure 3. Comparison of observed GPS coseismic displacements (Huang *et al*. 2017) to those of the finite-element model. Inset shows the fault geometry and slip distribution embedded within the FEM from the joint slip inversion from Huang *et al.* (2017). The EMC fault rupture is shown as a red line.

3 MODELING APPROACH

We use 5 yr of cumulative far-field postseismic displacements to constrain models for afterslip and viscoelastic relaxation. Afterslip models are based on an inversion of the postseismic data using a dislocation model, while viscoelastic relaxation is explored by forward modeling using a finite-element model (FEM) constrained by the postseismic observations. We do not compute models of poroelastic rebound as its influence is largely confined to the immediate near-field of an earthquake and it was found to make a minor contribution to the early post-EMC deformation by Gonzales-Ortega *et al.* (2014).

We begin the postseismic study by assuming that all postseismic deformation is due to afterslip. For this inversion, we keep the same dip angle and extend the eight-segment coseismic fault geometry proposed by Huang *et al.* (2017) from 15 km depth downward to 100 km depth (Fig. 4a) in order to account for hypothetical deep afterslip. The fact that these segments are dipping does not lead to a qualitative difference in our determination from models in which the segments have a vertical dip. Each fault segment is discretized into 800 4 km × 4 km subfaults, each allowed to slip along the fault plane with a rake between 135° and 225°, representing a right-lateral strike-slip-dominated motion with some up- or downdip components. The dislocation inversion approach, as well as model smoothing is described in Huang *et al.* (2017). We use the EDGRN/EDCMP code (Wang *et al.*2003) to compute the Green's functions in a layered elastic Earth

structure (Huang *et al.*2017), with the deepest layer extending to infinite depth.

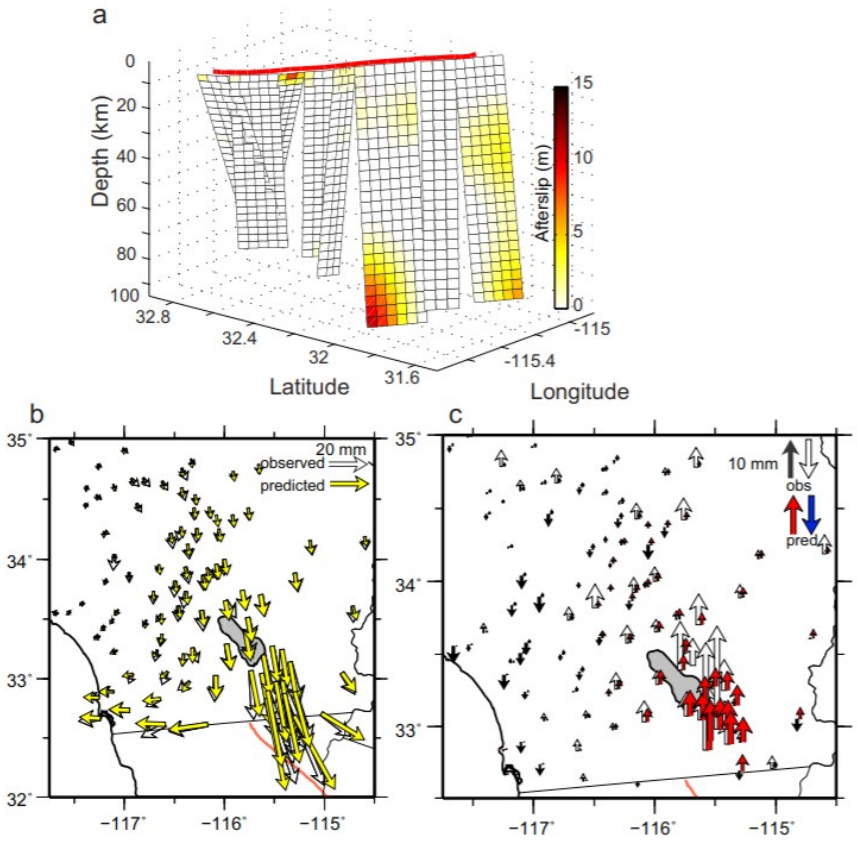

Figure 4. (a) Geometry used in afterslip elastic dislocation model along with the afterslip distribution obtained from the best-fit inversion of the postseismic displacements. (b) Comparison of GPS observed and calculated afterslip horizontal surface displacements. (c) Comparison of GPS observed and calculated afterslip vertical surface displacements.

To explore the role of viscoelastic relaxation in the postseismic displacements, we develop a 3-D FEM of the region using the software package ABAQUS (www.3ds.com) in order to test candidate Maxwellian viscoelastic rheologies of the lower crust and upper mantle (e.g. Freed *et al.*2006a, 2007). Matching the model predictions to the 5-yr total displacements obtained from the logarithmic fitting function provides us with an average viscosity structure over this time period. While many studies choose to use a Burger's rheology to fit displacement time-series, such an approach does not generally add any spatial information regarding rheologic strength, our primary objective. Our FEM first calculates coseismic stress changes based on the inferred coseismic slip distribution from Huang *et al.* (2017), then enables candidate viscoelastic rheologies to relax for 5 yr, allowing for a comparison of observed and calculated 5-yr cumulative displacements.

The central portion of the FEM mesh is shown in Fig. 5. The full model extends outward 1000 km from the EMC epicentre and to a depth of 250 km, sufficient distance such that imposed fixed boundary conditions do not

influence model results. We model a horizontally variable Moho depth based on tomographic models (Tape *et al.*2012; the background colour contours in Fig. 1a), which includes a thin, 23-km-thick crust in the Salton Trough that thickens to over 30 km beneath the Peninsular Ranges and other surrounding regions. Due to the decrease in seismic data coverage south of the US/Mexico border, we extrapolate the depth of the crust/mantle boundary along-strike assuming that these thicknesses are consistent throughout the Salton Trough and Baja Peninsula, however Ramirez-Ramos *et al.*(2015) show that the Moho may be even shallower beneath the Mexicali Valley and Laguna Salada basins than the Salton Trough of California. With no sharp deeper seismic reflectors in this region, we rely on the contours of the crust/mantle boundary to define the boundary between deeper rheologic layers within the mantle. This allows us to model deeper mantle layers with constant thicknesses.

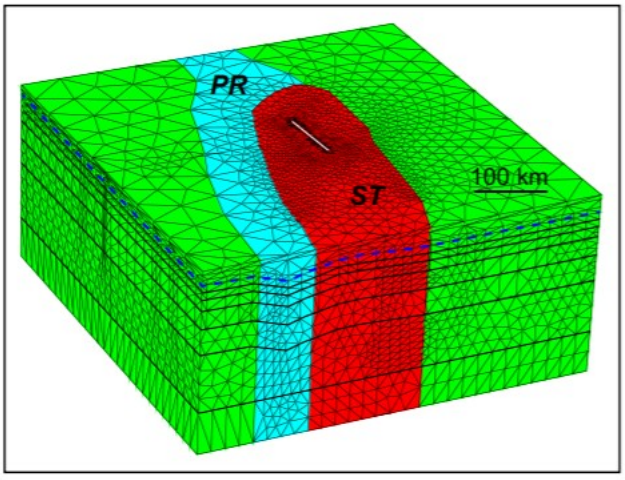

Figure 5. Central portion of the finite-element mesh used to calculate post-seismic surface displacements due to viscoelastic relaxation. Zones of similar rheological properties are separated by black lines; the blue dashed line is the Moho. PR—Peninsular Ranges. ST—Salton Trough.

The FEM assumes a depth-dependent elastic structure (Table 1) based on the Southern California Earthquake Center Community Velocity Model that is derived from observed seismic velocities (Wei *et al.*2011). We incorporate the rupture geometry from Huang *et al.* (2017; Fig. 3, inset), with each fault segment broken up into 2 km × 2 km patches to allow variation of coseismic slip and rake across each fault segment. Coseismic slip is simulated by the use of constraint equations that describe how the opposing sides of each patch move relative to each other. We incorporate the preferred coseismic slip distribution (Fig. 3, inset) from Huang *et al.*(2017). Because the coseismic inversion did not incorporate a depth-dependent elastic structure, while the FEM does, a modest a modest amount of slip at depth has to be added to the FEM to match the observed coseismic displacements (Fig. 3).

Table 1. The assumed elastic structure used in the postseismic afterslip inversions and FEM viscoelastic forward modeling.

Depth (km)	E (GPa)	ν
0–6.0	60	0.25
6.0–16.0	88	0.25
16.0–32.0	104	0.25
32.0–100.0	151	0.25

Table 2. Best-fitting models and their respective ssr.

Model number	Description	Horizontal ssr	Vertical *ssr*	Average ssr
1	Afterslip	2.28	3.14	2.57
2	Lower crustal flow	5.85	4.18	5.29
3	Mantle flow	3.16	3.37	3.23
4	Depth-dependent viscosity	2.90	3.17	2.99
5	Horizontally varying viscosity	3.08	3.30	3.15
6	Best-fitting 3-D viscosity structure	2.71	3.30	2.91

Both afterslip and viscoelastic models are scored by the sum of squared residuals (ssr) misfit given by

$$\text{ssr} = \sqrt{\frac{1}{n}\sum\frac{(x_o - x_p)^2}{\sigma^2}} \quad (3)$$

where n is the total number of observations, x_o and x_p are the observed and predicted surface displacements and σ is the observational error.

While scoring model results against observed geodetic observations provides a measure of the reasonableness of such models, the resulting so-called best-fitting model does not necessarily indicate the most accurate representation of the rheologic structure, as both the models and the data have limitations. Given these limitations, we refer to our favourite model as ‘the preferred model’. From the data side, a paucity of GPS stations south of the US border and in the vicinity of the rupture in particular, prevents a unique rheologic structure from being determined, especially with regards to trade-offs between afterslip and viscoelastic relaxation. From the modeling side, computational limitations do not allow us to more fully explore the parameter space, such as a wide range of layer thicknesses, lateral dimensions and viscosity values of each domain. Limitations of explorable model space required us to *a priori* choose a few discrete intervals where the rheologic structure varies both horizontally and vertically. Though such intervals are generally chosen based on thermal or seismic considerations, they are nevertheless somewhat arbitrary and thus limiting as to the conclusions we can draw from this study. Since the preferred models are thus not necessarily the most accurate representation, we follow the results section with a discussion of the plausibility of the preferred model by

comparing it to independently determined petrological models that describe where we might expect to see changes in viscosity based on temperature estimates and the onset of melting at depth. These are designed to augment the discussion of the plausibility of the preferred model, but cannot counter the non-uniqueness issues that one must consider when assessing the conclusions of this study.

4 RESULTS

The afterslip distribution determined by the elastic inversion to explain far-field postseismic displacements (Figs 4b and c) requires deep slip predominantly below 70 km (Fig. 4a) and suggests significant slip is required below 100 km depth. A model that only considers distributed afterslip provides a reasonable match to the data—it actually leads to a lower *ssr* misfit (Model 1 in Table 2) than any of the viscoelastic models discussed below. However, this is an implausible solution as it is unlikely that a fault could extend much beyond the lower crust, especially in a region marked by a high geotherm. This is also an implausible slip distribution for stress-driven afterslip, which predicts the largest slip immediately below the rupture, rapidly decaying with depth (e.g. Freed *et al.*2006b). Inversion models that do not allow afterslip to extend below the crust cannot account for displacements well north of the US border without greatly overpredicting displacements closer to the border. Such a model simply cannot account for the long wavelength of the postseismic deformation pattern. The inversion results demonstrate the need for deep postseismic deformation, most likely due to viscoelastic flow.

We do not rule out a contribution from afterslip to postseismic displacements, especially in the near-field (within 50 km of the fault). This is where shallow afterslip has its greatest influence on postseismic displacements (Gonzales-Ortega *et al.*2014). However, the paucity of GPS stations recording postseismic displacements in Mexico prevents such an assessment. While several stations were installed in Mexico between 6 months and a year after the earthquake, it is difficult to utilize in the present analysis time-series that have no measured interseismic velocities from before the earthquake and have missed the initial phase of postseismic deformation.

For the testing of viscoelastic relaxation models, we initially consider relatively simple candidate rheology structures, such as flow within a viscously uniform lower crust (with an elastic mantle) and within a viscously uniform mantle (with an elastic crust). For each configuration, we vary the assumed viscosity to determine the best-fitting model. The best-fitting lower crustal flow model (5×10^{18} Pa·s) cannot match displacements at stations more than 100 km from the epicentre without greatly overpredicting displacements at stations closer to the epicentre. In addition, such models lead to subsidence in the Salton Sea region where postseismic uplift is observed. Thus, even the best-fitting lower crustal flow model leads to a poor

fit of the observed displacements (Model 2 in Table 2). The best-fitting uniform mantle flow model (10^{19} Pa·s) leads to a much better fit to the observed displacements. It can reasonably fit the horizontal deformation pattern, though with modest errors in azimuth, and greatly improved matching of vertical displacements, capturing the general trend of uplift in the region. This is reflected in a much-reduced misfit (Model 3 in Table 2) compared to the lower crustal flow model.

We next consider depth-dependent, but still horizontally uniform, rheologies, enabling a combination of lower crustal flow and mantle flow that varies with depth. The best-fitting depth-dependent model consists of a strong lower crust (10^{20} Pa·s), overlying a 10-km-thick, stronger mantle lid (8×10^{20} Pa), that caps a much weaker asthenosphere (10^{19} Pa·s) extending to a depth of ~100 km, and then modestly weaker (5×10^{18} Pa·s) mantle below, provides a modestly reduced misfit to the data (Model 4 in Table 2 and Fig. 6) compared to the uniform mantle model. We next explore horizontal varying rheologies, where the viscosity of the crust and mantle can vary between the Salton Trough and the surrounding regions (Peninsular Ranges), though neither layer is depth dependent. The best-fitting model for this configuration has a lower crust that is strong throughout (>10^{20} Pa·s) and a mantle that is modestly weaker beneath the Salton Trough (7×10^{18} Pa·s) compared to the outlying regions (10^{19} Pa·s). This model has greater misfit (Model 5 in Table 2 and Fig. 6) than the depth-dependent model, though it represents a modest improvement over the uniform mantle flow model, suggesting the depth-dependence is more important than horizontal heterogeneity.

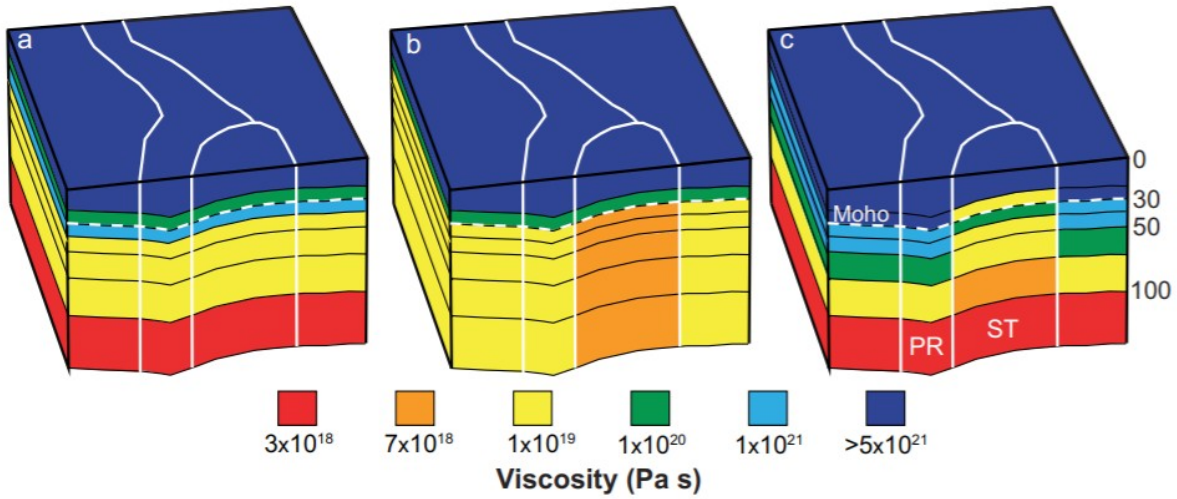

Figure 6. Viscosity structures of (a) Model 4, (b) Model 5 and (c) Model 6 (our preferred model, see the text). PR—Peninsular Ranges and ST—Salton.

Our preferred model is one that considers both a depth-dependent and horizontally varying viscosity structure. This model has a weak lower crust within the Salton Trough (10^{19} Pa·s), underlain by a strong 10-km-thick mantle lid (10^{20} Pa·s), with viscosity then decreasing with depth to

3×10^{18} Pa·s at a depth of 90 km (Model 6 in Table 2 and Fig. 6). Outside the Salton Trough a strong lower crust and mantle lid (10^{21} Pa·s) overlie a mantle in which the viscosity decreases steadily, eventually reaching the same low viscosity of 3×10^{18} Pa·s at 90 km depth as beneath the Salton Trough. Figs 7(a) and (b) show a comparison between observed and calculated horizontal and vertical postseismic displacements, respectively, and Figs 7(c) and (d) show the corresponding residual displacements (observed minus calculated). This 3-D heterogeneous model leads to the minimal misfit with respect to the observed data (Model 6 in Table 2) for all candidate rheologies we considered. The most significant misfit is associated with observed vertical displacements that show significant variations between closely spaced stations. Such variations are likely associated with non-tectonic processes or local tectonic processes.

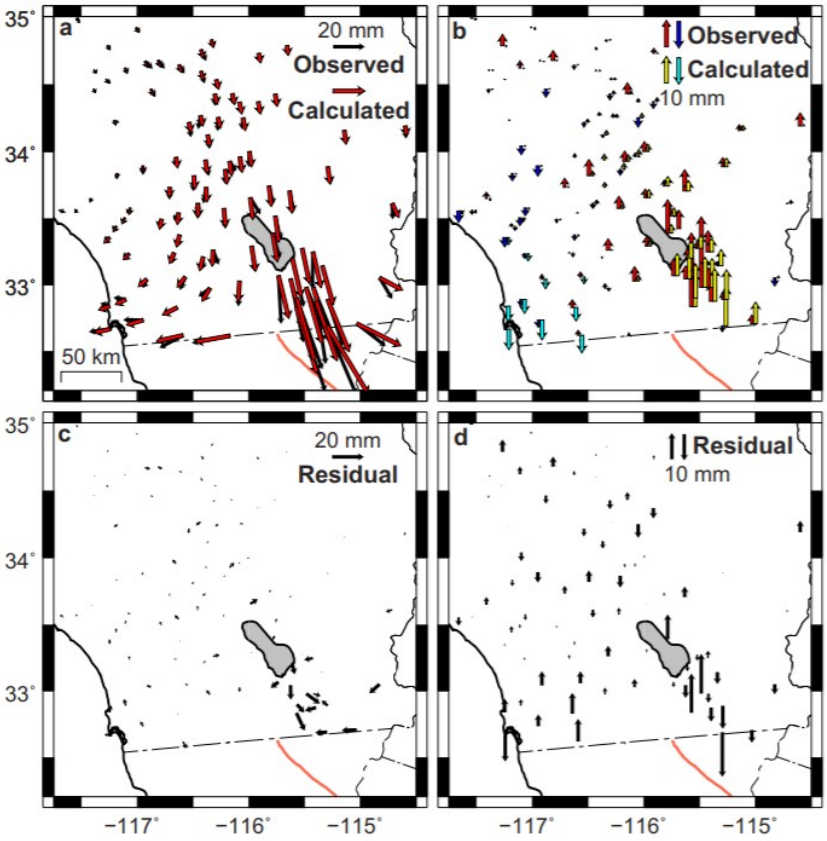

Figure 7. Comparison between observed and calculated (a) horizontal and (b) vertical postseismic displacements. (c) Horizontal and (d) vertical residual displacements (observed minus calculated).

Fig. 8 shows how the ssr misfit (normalized to the best-fit model) varies as a function of changing the viscosity of one region with all other regions held fixed. The misfit is most sensitive to deviations in the viscosity of the lower crust and mantle lid beneath the Salton Trough. This results from the viscosity of these regions having the greatest influence on vertical displacements in the region.

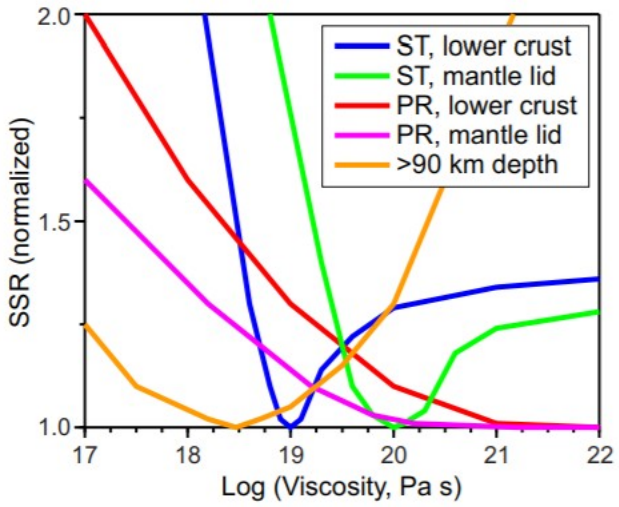

Figure 8. Misfit (ssr) normalized to the best-fitting model (Fig. 6) as a function of varying the viscosity in different regions of the model. This illustrates how the misfit increases if we change the viscosity within a region while holding all other viscosities constant.

5 DISCUSSION

postseismic displacements have previously been explained using a homogenous crust over a mantle half-space horizontally varying between the Salton Trough and outlying regions (Pollitz *et al.*2012). We find that the lower crustal viscosity must also vary horizontally across this region to simultaneously explain both horizontal and vertical observed postseismic displacements (Fig. 7). A lower crust with similar viscoelastic strength beneath both the Peninsular Ranges and Salton Trough is unlikely considering the large difference in heat flow (~40 mW m^{-2} in the Peninsular Ranges compared to >100 mW m^{-2} in the Salton Trough, Blackwell *et al.*2011) and evidence for melt beneath the Salton Trough from ambient-noise tomography (Barak *et al.*2015) and recent volcanoes (Schmitt & Vazquez 2006).

Our inference of a viscously weaker lower crust beneath the Salton Trough is consistent with the modeling results of Rollins *et al.* (2015). However, their study suggests that the extent of the lower viscosity zone is localized to the area of geothermal activity that spans only about one-third of the width of the trough. While we cannot rule out this possibility, high heat flow is observed throughout the Salton Trough (Lachenbruch *et al.*1985; Blackwell *et al.*2011), implying the entire lower crust in this region should be of relatively uniform viscosity (unless it has a horizontally varying composition or degree of melting).

If we define a mechanical lithosphere as the region in which stresses do not significantly relax in the time frame of observed postseismic deformation (several years), this would approximately correspond to domains with viscosities greater than ~10^{20} Pa·s in our models. For the Peninsular Ranges and other regions outside of the Salton Trough, this corresponds to a

mechanical LAB at about ~65 km depth in our model (Fig. 9b). The seismic LAB is often defined as the depth of the largest amplitude drop in shear wave velocities. Analysis of *Sp* receiver functions beneath the Peninsular Ranges suggests a seismic LAB at ~80 km depth (Lekic *et al.*2011), 15 km deeper than the inferred mechanical LAB. A similar difference is found beneath the Salton Trough, where the mechanical LAB in our study is found to occur at ~32 km depth (with an intervening weak lower crust), while the seismic LAB is found to be at ~44 km depth (Lekic *et al.*2011, Fig. 9d).

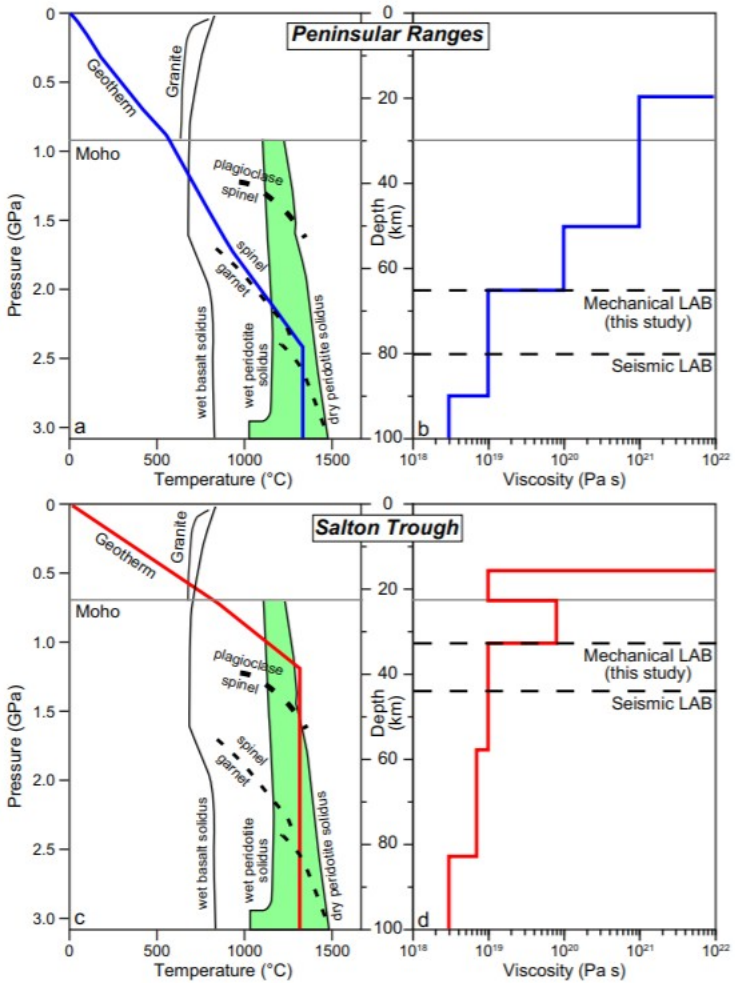

Figure 9. (a) and (c) Calculated geothermal gradient and mantle melting curves and phase changes (see the text) for the Peninsular Ranges and Salton Trough, respectively. (b) and (d) Our best-fit viscosity structure for the Peninsular Ranges and Salton Trough, respectively. Moho depths are from Tape *et al.* (2012) and the seismic LABs are from Lekic *et al.* (2011). Mechanical LAB (see the text for definition) from our study. The green region represents the range of conditions for melting based on the water content of the mantle.

The difference in depth between the mechanical and the seismic LABs is not unexpected, as each is based on a different set of observations (shear wave velocities versus postseismic surface displacements), a different timescale (seconds versus months to years), and a different type of loading (passage of transient seismic waves versus static stress changes). On the other end of

the LAB spectrum would be that inferred from coherence analysis of gravity and topography (Lowry & Pérez-Gussinyé 2011), which suggests an LAB depth in these regions of only about 5 km at long-term geological timescales (i.e. thousands to millions of years for crustal and mantle rocks to relax). These systematic differences in the inferred depth of the LAB are thus consistent with the timescale of each type of constraining observations (e.g. Thatcher & Pollitz 2008). Evidently, the depth of the LAB depends greatly on how one defines and observes it.

To see how our inferred viscosity structure compares to the inferred depth-dependent thermal structure of the region (e.g. Dickinson & Freed 2014), we calculate a geotherm based on the observed surface heat flow and then estimate the depth of melting using experimentally calibrated melting curves for wet granite (Pattison *et al.* 2003), wet basalt (Moyen 2011) and wet and dry peridotite (Green 2015). We calculate a steady-state conductive geotherm for the Peninsular Ranges (Fig. 9a) and Salton Trough (Fig. 9c) following the methodology of Chapman (1986),

$$T\ (z) = T_t + \frac{q_t}{k}\Delta z - \frac{\rho H}{2k}\Delta z^2 \text{ and } q_b = q_t - \rho H \Delta z \qquad (4)$$

where T represents the temperature (°C), q is the heat flow (mW m^{-2}), the subscripts t and b indicate the top and bottom of a layer, respectively, k is the thermal conductivity (Wm^{-1} K^{-1}), ρH represents the volumetric heat production (μW m^{-3}) and Δz is the thickness of the layer (m). Our temperature-dependent crustal thermal conductivity is calculated using the equations of Sass *et al.*(1992), whereas the temperature-dependent mantle thermal conductivity is calculated with the equations of Jaupart & Mareschal (1999). This is done iteratively by recalculating the thermal conductivity at different temperatures and substituting this value into eq. (3). We assume that internal heat production varies exponentially with depth for the crust and assume a constant internal heat production value of 0.03 μW m^{-3} (Rudnick *et al.*1998) for the mantle. Our conductive steady-state geotherm ends at a potential temperature of 1300 °C, where it assumes an adiabatic gradient of 0.4 °C km^{-1}.

This extrapolation of geothermal gradients to depth is estimated to be in error by as much as 15 per cent at lower crustal depths (Eppelbaum *et al.*2014). Our modeled geotherm is fixed by our choices of internal heat production, temperature at the Moho and the accuracy of surface heat flow measurements. We are also neglecting advection of heat by fluids, which is clearly important at least locally in the geothermal fields. Of these, surface heat flow is the best constrained, and Moho temperature is the least constrained. For our simple models, 15 per cent error corresponds to a temperature range between 457 °C and 619 °C at the Moho for the Peninsular Ranges batholith, and 730 °C and 956 °C for the Salton Trough. Thus, our geotherms are rough approximations that may be in error by 200 °C –300 °C at mantle depths.

To model mantle melting, we consider the wet basalt solidus as the minimum temperature at which melting could initiate. Hydrated pyroxenite and eclogite are potential upper mantle melting sources because pyroxenites are very common among xenolith assemblages in the Sierra Nevada Mountains (Ducea & Saleeby 1996) and the Mojave Desert (e.g. Wilshire 1990). They are interpreted to be ultramafic residues produced during batholith differentiation. Thus, similar rocks may be present in the upper mantle beneath the Peninsular Ranges batholith. To simulate a range of hydration and carbonation conditions within the upper mantle, we use the wet and dry melting curves for peridotite (Green 2015). Pyroxenite and eclogite will melt at temperatures between the wet basalt solidus and the peridotite solidus, with more refractory bulk compositions melting at higher temperatures (Pertermann & Hirschman 2003). The results of our two geotherm models with pertinent melting reactions and phase changes are shown in Figs 9(a) and (c) for both wet and dry conditions.

Beneath the Peninsular Ranges, the depth of our inferred mechanical LAB (65 km depth in Fig. 9b) corresponds with the depth just above where the geotherm crosses the wet melting curve of peridotite (Fig. 9a). Similarly, beneath the Salton Trough the depth of our mechanical LAB (32 km depth in Fig. 9d), corresponds with the depth where the geotherm crosses the wet peridotite melting curve (Fig. 9c). Thus, the depth of the inferred onset of wet melting corresponds with the depth of our inferred mechanical LAB throughout the region, despite significant changes in temperatures.

Within the crust beneath the Peninsular Ranges, our geotherm does not intersect the minimum melting curves for granite or wet basalt (Fig. 9a), which cover a range of potential lower crustal compositions. This implies there is no melt present within the lower crust of the Peninsular Ranges, consistent with our inferred viscously strong lower crust (Fig. 9b). In contrast, our geotherm beneath the Salton Trough does intersect the minimum melting curves for granite and wet basalt (Fig. 9c), implying partial melting in the lower crust. Our inference of partial melting in the lower crust is supported by the presence of Quaternary volcanism within the trough and the presence of granitic- and amphibole-bearing basalt xenoliths with U–Th isochron ages between 9 and 30 ka (Schmitt & Vazquez 2006). Barak *et al.* (2015) inferred from seismic imaging the presence of between 4.5 and 6 per cent partial melt beneath the Salton Trough. Thus, the low-viscosity lower crust beneath the Salton Trough is likely the result of the presence of partial melt and high temperatures (Fig. 9d). The presence of a well-defined mantle lid beneath the Salton Trough is consistent with the presence of a refractory, dry peridotite, produced by extraction of mafic melts that formed the lower crust within the Salton Trough (e.g. Lachenbruch *et al.*1985). Our inference of mantle melt below the Salton Trough lithosphere is consistent with seismic shear wave splitting data showing large splitting times and fast directions aligned with the plate

boundary only below this region, which Barak *et al.* (2015) interpret as vertical melt zones parallel to the shear direction in the uppermost mantle.

Our inferred viscosity for the lower crust beneath the Peninsular Ranges is about two orders of magnitude greater than that of the lower crust beneath the Salton Trough. We can explore the cause of this difference by utilizing the relationship for effective viscosity, η, given by

$$\eta = \frac{\sigma^{1-n} \exp(Q/RT)}{2A \ f_{H_2O}{}^r \exp(\alpha\phi)} \quad (5)$$

where σ is the total differential stress, Q is the activation energy, R is the Universal Gas Constant, T is absolute temperature, A is an experimental constant, f_{H2O} is the water fugacity, r is the water fugacity exponent, α is a melt fraction parameter and ϕ is the melt fraction. The temperature of the lower crust beneath the Peninsular Ranges is ~500 °C (Fig. 9a), compared to ~700 °C beneath the Salton Trough (Fig. 9c). For this given temperature difference (all other parameters being equal), the two-order-of-magnitude difference in the lower crustal viscosity can be explained by an activation energy of 144 kJ $mol^{-1}$for rocks beneath the Salton Trough. This approximately corresponds to the activation energy ranges of Westerly Granite, Quartzite and Aplite (Kirby & Kronenberg 1987), which would require a felsic lower crust. More mafic materials, such as diabase have higher activation energies (Kirby & Kronenberg 1987) that would lead to a much greater change in viscosity (three orders of magnitude) given the temperature differences. Since the lower crust beneath the Salton trough is inferred geophysically (Barak *et al.*2015) and petrologically (Schmitt & Vazquez 2006) to be composed of mafic rocks, the viscosity difference must be influenced by more than just variation in temperature.

The presence of melt in the lower crust beneath the Salton Trough would also serve to lower the viscosity. Recent experiments on granulite (Zhou *et al*. 2017) and gabbro (Zhou *et al.*2012) show significant decreases in rock strength with increasing melt fraction. The effects of melt fraction on strain rate can be estimated using the experimentally derived equation for gabbro (Zhou *et al.*2012):

$$\dot{\epsilon} = \dot{\epsilon}_{(0)} \exp(128(\phi - \phi_{(0)})), \quad (6)$$

where

$\epsilon^{\cdot}$ is the strain rate, $\epsilon^{\cdot}(0)\langle sy\rangle$ is the strain rate prior to melting, ϕ is the melt fraction and $\phi_{(0)}$is the initial melt fraction, which is zero for our calculations. Using the geophysically inferred melt fractions in the Salton Trough lower crust of 4–6 per cent (Barak *et al.*2015) results in a 2–3 order of magnitude increase in strain rate, assuming only the melt fraction varies, consistent with the two order of magnitude decrease in viscosity predicted by our models. Thus, the low viscosity beneath the Salton trough is best explained by high temperatures that induce partial melting in a mafic lower crust.

The viscosity structures of the mantle beneath the Peninsular Ranges and the Salton Trough generally follow the difference in thermal gradients and predicted depths to melting. The mantle lid viscosity (10^{20} Pa·s) beneath the Salton Trough corresponds to temperatures less than ~1000 °C . At temperatures above ~1000 °C, our calculated geotherm intersects the wet peridotite solidus (Fig. 9c), corresponding to the inferred decrease in viscosity at the base of the mantle lid (Fig. 9d). Similarly, beneath the Peninsular Ranges, the geotherm intersects the wet peridotite solidus at ~70 km depth (Fig. 9a), just slightly deeper than the inferred viscosity decrease from 10^{20} to 10^{19} Pa·s (Fig. 9b). This suggests that the onset of partial melting in peridotite may control the depth to the base of the mechanical lithosphere. The onset of melting may have been too gradual to produce a sharp enough impedance contrast to be imaged with receiver function. Thus, the presence of a clearly defined, shallow thin mantle lid beneath the hotter Salton trough, and its absence beneath the cooler Peninsular Ranges, suggests there are likely compositional differences in the shallow parts of the mantle. Furthermore, if there is a difference in water content between the two mantles, its influence on viscosity is much smaller than the influence of temperature. In both cases, the depth to the base of the seismic lithosphere is deeper than the predicted depths of the onset of partial melting, but occurs where our thermal models suggest the geotherm becomes adiabatic. This may indicate an increase in the partial melt percentage associated with the change from a conductive to an adiabatic geotherm.

6 CONCLUSIONS

We use 5 yr of observed cumulative GPS postseismic surface displacements to constrain FEMs of viscoelastic relaxation following the 2010 EMC earthquake. Our results suggest that the postseismic deformation pattern is well explained by a horizontally varying and depth-dependent viscosity structure under the Salton Trough, where our models infer a relatively weak (10^{19} Pa·s) lower crust underlain by a stronger mantle lid ($\geq 10^{20}$ Pa·s). The lower crust beneath the Peninsular Ranges is inferred to have a high viscosity ($\geq 10^{20}$ Pa·s). The uppermost mantle beneath the Peninsular Ranges is inferred to be much stronger than the uppermost mantle beneath the Salton Trough, with the viscosity of both regions decreasing with depth until they converge at 3×10^{18} Pa·s at ~90 km depth.

We find that the two-orders-of-magnitude higher viscosity inferred for the lower crust beneath the Peninsular Ranges compared to the viscosity of the lower crust beneath the Salton Trough is primarily due to the 200 °C temperature difference, which induces partial melting in the mafic lower crust of the Salton Trough. The viscosity differences between the Salton Trough and Peninsular Ranges are strongly correlated with temperature differences between the two regions, except for the presence of a mantle lid beneath the Salton Trough, which implies that the upper mantle beneath the Peninsular Ranges and Salton Trough are compositionally distinct. Variation

in the geothermal gradient across these distinct lithospheric blocks induces partial melting within the lower crust and in the mantle at a depth of ~32 km beneath the Salton Trough, whereas melting is not inferred to begin until a depth of ~65 km beneath the Peninsular Ranges. This may be a result of the mechanical LAB being correlated with the predicted depths of the onset of wet partial melting of peridotite. In contrast, the seismic LAB may correspond with an increase in the partial melt percentage associated with the change from a conductive to an adiabatic geotherm.

Acknowledgements

We thank Douglas Dreger for providing the codes for afterslip modeling. We thank Kelin Wang and Whitney Behr for comments and suggestions that greatly improved this manuscript. Part of this research was supported by the National Aeronautics and Space Administration (NASA) Earth Surface and Interior focus area and performed at the Jet Propulsion Laboratory, California Institute of Technology. M-HH was supported by an appointment to the NASA Postdoctoral Program at the Jet Propulsion Laboratory, administered by Oak Ridge Associated Universities through a contract with NASA. This material is based on EarthScope Plate Boundary Observatory data services provided by UNAVCO through the GAGE Facility with support from the National Science Foundation (NSF) under NSF cooperative agreement no. EAR-1261833 and NASA.

REFERENCES

Barak, S., Klemperer, S.L. & Lawrence, J.F., 2015. San Andreas Fault dip, Peninsular Ranges mafic lower crust and partial melt in the Salton Trough, Southern California, from ambient-noise tomography, Geochem. Geophys. Geosyst., doi:10.1002/2015GC005970.

Blackwell, D.D., Richards, M.C., Frone, Z.S., Batir, J.F., Williams, M.A., Ruzo, A.A. & Dingwall, R.K., 2011. SMU Geothermal Laboratory Heat Flow Map of the Conterminous United States, 2011. Available at: http://www.smu.edu/geothermal.

Chapman, D.S., 1986. Thermal gradients in the continental crust, in: The Nature of the Lower Continental Crust, eds Dawson, J.B., Carswell, D.A., Hall, J. & Wedepohl, K.H. Vol. 24, pp. 3946–3972, Geol. Soc. Spec. Publ.

Dickinson, H. & Freed, A.M., 2014. Inferring mantle rheology in Western Nevada using postseismic relaxation and Lake Lahontan Rebound, in Proceedings from the Annual Meeting of the American Geophysical Union, San Francisco, California.

Ducea, M.N. & Saleeby, J.B., 1996. Buoyancy sources for a large, unrooted mountain range, the Sierra Nevada, California: evidence for xenolith thermobarometry, J. geophys. Res., 101, 9229–8244.

Eppelbaum, L., Kutasov, I. & Pilchin, A., 2014. Applied Geothermics, in Lecture Notes in Earth System Sciences, Springer-Verlag Berlin Heidelberg, doi:10.1007/978-3-642-34023-9_1.

Fletcher, J.M. et al., 2014. Assembly of a large earthquake from a complex fault system: surface rupture kinematics of the 4 April 2010 El Mayor-Cucapah (Mexico) Mw 7.2 earthquake, Geosphere, 10, doi:10.1130/GES00933.1.

Freed, A.M., Burgmann, R., Calais, E., Freymueller, J. & Hreinsd ¨ ottir, S., ´ 2006a. Implications of deformation following the 2002 Denali, Alaska, earthquake for postseismic relaxation processes and lithospheric rheology, J. geophys. Res., 111, doi:10.1029/2005JB003894.

Freed, A.M., Burgmann, R., Calais, E. & Freymueller, J., 2006b. Stress- ¨ dependent power-law flow in the upper mantle following the 2002 Denali, Alaska, earthquake, Earth planet. Sci. Lett., 252, 481–489.

Freed, A.M., Burgmann, R. & Herring, T., 2007. Far-reaching transient mo- ¨ tions after Mojave earthquakes require broad mantle flow beneath a strong crust, Geophys. Res. Lett., 34, L19302, doi:10.1029/2007GL030959.

Gonzalez-Ortega, A. et al., 2014. El Mayor-Cucapah (Mw 7.2) earthquake: early near-field postseismic deformation from InSAR and GPS observations, J. geophys. Res., 119, doi:10.1002/2013JB010193.

Green, D.H., 2015, Experiment petrology of peridotites, including effects of water and carbon on melting in the Earth’s upper mantle, Phys. Chem. Minerals, 42, 95–122.

Hines, T.T. & Hetland, E.A., 2016. Rheologic constraints on the upper mantle from 5 years of postseismic deformation following the El Mayor-Cucapah earthquake, J. geophys. Res., 121, 6809–6827.

Huang, M-H., Fielding, E.J., Dickinson, H., Sun, J., Gonzalez-Ortega, J.A., Freed, A.M. & Burgmann, R., 2017. Fault geometry inversion and slip ¨ distribution of the 2010 Mw 7.2 El Mayor-Cucapah earthquake from geodetic data, J. geophys. Res., 122, 607–621.

Jaupart, C. & Mareschal, J.C., 1999. The thermal structure and thickness of continental roots, Lithos, 48(93), 93–114.

Kirby, S.H. & Kronenberg, A.K., 1987. Rheology of the lithosphere; selected topics, Rev. Geophys., 25, 1219–1244.

Lachenbruch, A.H., Sass, J.H. & Galanis, S.P., 1985. Heat flow in southernmost California and the origin of the Salton Trough, J. geophys. Res., 90(B8), 6709–6736.

Lekic, V., French, S.W. & Fischer, K.M., 2011. Lithospheric thinning beneath rifted regions of Southern California, Science, doi:10.1126/science/1208898.

Lowry, A.R. & Perez-Gussiny ´ e, M., 2011. The role of crustal quartz in ´ controlling Cordilleran deformation, Nature, 471, 353–357.

Moyen, J-F., 2011. The composite Archaean grey gneisses: petrological significance, and evidence for a non-unique tectonic setting for Archaean crustal growth, Lithos, 123, 21–36.

Pattison, D.R.M., Chacko, T., Farquhar, J. & McFarlane, C.R.M., 2003. Temperatures of granulite-facies metamorphism: constraints from experimental phase equilibria and thermobarometry corrected for retrograde exchange, J. Petrol., 44, 867–900.

Pertermann, M. & Hirschmann, M.M., 2003. Partial melting experiments on a MORB-like pyroxenite between 2 and 3 GPa: constraints on the presence of pyroxenite in basalt source regions from solidus location and melting rate, J. geophys. Res., 108(B2), doi:10.1029/2000JB000118.

Pollitz, F.F., Burgmann, R. & Thatcher, W., 2012. Illumination of rheological ¨ mantle heterogeneity by the M7.2 2010 El Mayor-Cucapah earthquake, Geochem. Geophys. Geosyst., 13, Q06002, doi:10.1029/2012GC004139.

Ramirez-Ramos, E.E., Vidal-Villegas, A., Gonzalez-Fern ´ andez, A. & ´ Stock, J.M., 2015. A crustal velocity model for the Southern Mexicali Valley, Baja California, Mexico, Seismol. Res. Lett., 86, 181– 191.

Rollins, C., Barbot, S. & Avouac, J-P., 2015. Postseismic deformation following the 2010 M = 7.2 El Mayor-Cucapah earthquake: observations, kinematic inversions and dynamic models, Pure appl. Geophys., 172, doi:10.1007/s00024-014-1005-6.

Rudnick, R.L., McDonough, W.F. & O'Connell, R.J., 1998. Thermal structure, thickness and composition of continental lithosphere, Chem. Geol., 145, 395–411.

Sass, J.H., Lachenbruch, A.H., Moses, T.H., Jr. & Morgan, P., 1992. Heat flow from a scientific research well at Cajon Pass, California, J. geophys. Res., 97, 5017–5030.

Schmitt, A.K. & Vazquez, J.A., 2006. Alteration and remelting of nascent oceanic crust during continental rupture: evidence from zircon geochemistry of rhyolites and xenoliths from the Salton Trough, California, Earth planet. Sci. Lett., 252, 260–274.

Tape, C., Plesch, A., Shaw, J.H. & Gilbert, H., 2012. Estimating a continuous Moho surface for the California unified velocity model, Seismol. Res. Lett., 83, 728–735.

Thatcher, W. & Pollitz, F.F., 2008. Temporal evolution of continental lithospheric strength in actively deforming regions, GSA Today, 18(4–5), doi: 10.1130/GSAT01804.

Wang, R., Lorenzo Mart´ın, F. & Roth, F., 2003. Computation of deformation induced by earthquakes in a multi-layered elastic crust-FORTRAN programs EDGRN/EDCMP, Comput. Geosci., 29, 195–207.

Wei, S. et al., 2011. Superficial simplicity of the 2010 El MayorCucapah earthquake of Baja California Mexico, Nat. Geosci., 4, 615– 618.

Wei, S., Helmberger, D., Wen, S.O., Graves, R.W., Hudnut, K.W. & Fielding, E.J., 2013. Complementary slip distributions of the largest earthquakes in the 2012 Brawley swarm, Imperial Valley, California, Geophys. Res. Lett., 40, 847–852.

Wei, S. et al., 2015. The 2012 Brawley swarm triggered by injection-induced aseismic slip, Earth planet. Sci. Lett., 422, 115–125.

Wilshire, H.G., 1990. Lithology and evolution of the crust-mantle boundary region in the southwestern Basin and Range province, J. geophys. Res., 95, 649–665.

Zhou, Y., Zhang, H., Yao, W.Y., Dang, J. & He, C., 2017. An experimental study on creep of partially molten granulite under high temperature and wet conditions, J. Asian Earth Sci., 39, 15–29.

Zhou, Y., Rybacki, E., Wirth, R., He, C. & Dresen, G., 2012.Creep of partially molten fine-grained gabbro under dry conditions, J. geophys. Res., 117, B05204, doi:10.1029/2011JB008646.